

Bending-strain effects in conventional superconductors and superconducting junctions

Kjell S. Heinrich,¹ Henning G. Hugdal,¹ Morten Amundsen,¹ and Sol H. Jacobsen^{1,*}

¹*Center for Quantum Spintronics, Department of Physics, NTNU,
Norwegian University of Science and Technology, NO-7491 Trondheim, Norway*

We consider the effect of bending-strain in thin films of clean, conventional superconductors (S), and the proximity-induced effect of this strain in SN bilayers with a normal metal (N), and SNS junctions with equal curvatures in each superconductor. We find that the effective spin-orbit coupling due to strain in the superconductor induces both spin-polarized and unequal-spin even-frequency p-wave triplet pairings throughout the superconductor. When interfaced with a normal metal, additional odd-frequency pairings are induced, and their magnitudes can be tuned with the strain. In SNS junctions, the strain alone can induce a superconducting spin current in the junction. The spin-polarized current can undergo a $0 - \pi$ -transition, resulting in an in-plane, strain-induced magnetization that switches sign as a function of the strain. We discuss the underlying physics and its implications for superconducting spintronics.

I. INTRODUCTION

Conventional superconductors exist in plentiful elemental or alloyed form, and have been studied for decades, but their response to different stimuli – on their own or in conjunction with other materials – continue to provide novel fundamental insights. Deforming a superconducting wire or film results in bending-strain, and sometimes torsion, and will typically degrade the critical current that the superconductor can support, up to some critical value of strain beyond which the superconductivity breaks down altogether¹⁻³. However, recent studies have shown that bending-strain, sometimes referred to as curvature-induced strain in the literature, can also have profound effects on the superconductivity when applied in a material adjacent to the superconductor, through its modulation of the proximity effect⁴⁻⁸. These studies have shown that the effective spin-orbit coupling (SOC) introduced by curvature is instrumental in converting conventional s-wave, even-frequency, spin-singlet correlations into spin-polarized triplet correlations. Achieving spin-polarized superconducting correlations from abundant and versatile materials is highly desirable in order to, for example, combine zero-resistance currents with spin-manipulation for spintronic devices⁹⁻¹².

Modulation of the singlet order parameter occurs under the effect of SOC, an external magnetic field or an internal exchange field. When a superconductor is proximity-coupled to a ferromagnet or antiferromagnet, or exposed to an external magnetic field, odd-frequency, s-wave *spin-polarized triplet* correlations can be generated. That is, the generation of these correlations requires both spin-splitting and a second spin-orienting field, typically engineered via magnetic multilayers^{10,13,14} or by employing intrinsic SOC (for example from a heavy metal) in combination with a single exchange field¹⁵⁻¹⁷. Recent studies have shown that geometric curvature, increasingly harnessed for its advantages in spintronics¹⁸⁻²⁵, is an effective way to both design and manipulate curvature-induced SOC. Geometric curvature alone is therefore sufficient to affect the symmetries of superconducting correlations persisting in single magnetic elements *i.e. without using any intrinsic SOC, magnetic multilayers or strain*⁴⁻⁸. The addition of bending-strain may then be used to manipulate the different superconductivity populations in-situ, for example to control the superconducting transition^{5,8},

or the direction of Josephson current^{4,6}.

In contrast to its role in magnetic materials, geometric curvature *alone* (i.e. curvature without strain) is not expected to affect the symmetries of the order parameter of a plain s-wave superconductor. With ballistic transport, an interface with a normal metal (N) will convert a portion of the even-frequency, s-wave singlet correlations into odd-frequency p-wave singlets²⁶. When proximity-coupled to a non-magnetic material such as a semiconductor, normal metal or topological insulator, geometric curvature in the non-magnetic material can then affect the singlet order parameter in the presence of SOC, due to its tunable effect on the generation of unpolarised triplet correlations^{27,28}. For example, curvature in a proximity-coupled topological insulator, which has strong SOC, can induce topological superconductivity²⁹. Spin-orbit-coupled superconducting wires have also been found to display the evolution of topological phases themselves due to geometric deformation³⁰. Bending-strain introduces an effective SOC with a rotating normal vector. While of Rashba-type, the rotating angle affects the generation and modulation of triplet correlations differently from a constant, intrinsic Rashba-SOC, or extrinsic SOC from gating. In this article, we explore the extent to which bending-strain affects the symmetries of the order parameter in a conventional, even-frequency s-wave spin-singlet superconductor alone, and we examine the implications of the symmetry transformations on the proximity effect with normal metals in bilayers and Josephson junctions.

We will use the Bogoliubov-de Gennes framework³¹ to examine how the effective SOC of bending-strain in clean, conventional superconductors (S) can modulate the symmetries of the order parameter, and we therefore begin by introducing the curvilinear framework and discretizing and diagonalizing the continuum Hamiltonian in Section II. We go on to show how this combines with symmetry-modulations from normal-metal interfaces in SN bilayers and SNS Josephson junctions in Section III. We find that bending-strain in the superconductor gives an effective SOC that generates even-frequency p-wave triplets, both with and without spin polarization. In bilayers, the magnitude of the additional odd-frequency pairings can be tuned with the strain, and we find an in-plane, strain-induced magnetization that switches sign as a function of the strain in SNS junctions. We conclude by discussing the potential

benefits for superconducting spintronic devices in Section IV.

II. THEORY

We introduce geometric curvature in superconductors using the Frenet-Serret frame in Section II A, and define the continuum Hamiltonian with curvature-induced bending-strain in Section II B. We discretize the Hamiltonian to give the tight-binding model in Section II C. In Section II D, we define the s- and p-wave singlet and triplet amplitudes, as well as the density of states and spin magnetization as observables.

A. Frenet-Serret frame

We parametrize a curved superconductor using $\mathbf{R}(s, n, b) = \mathbf{r}(s) + n\hat{\mathcal{N}}(s) + b\hat{\mathcal{B}}(s)$, where $\mathbf{r}(s)$ characterizes the curve along the arclength s , and the parameters n , and b are the normal and binormal coordinates, respectively. The orthonormal basis vectors for the parametrization are the tangential $\hat{\mathcal{T}}$, normal $\hat{\mathcal{N}}$ and binormal $\hat{\mathcal{B}}$ directions, as illustrated in Fig. 1.

The Frenet-Serret formulas, which describe the change of the curvilinear unit vectors \hat{e}_μ , can be summarized as

$$\begin{pmatrix} \partial_s \hat{\mathcal{T}}(s) \\ \partial_s \hat{\mathcal{N}}(s) \\ \partial_s \hat{\mathcal{B}}(s) \end{pmatrix} = \begin{pmatrix} 0 & \kappa(s) & 0 \\ -\kappa(s) & 0 & 0 \\ 0 & 0 & 0 \end{pmatrix} \begin{pmatrix} \hat{\mathcal{T}}(s) \\ \hat{\mathcal{N}}(s) \\ \hat{\mathcal{B}}(s) \end{pmatrix}. \quad (1)$$

Here we have introduced the geometric curvature function $\kappa(s)$, which for a uniform curve is simply the inverse of the radius of the curve (see Fig. 1). Using Eq. (1), we can write the basis vectors as derivatives of $\mathbf{R}(s, n, b)$. We express them as $e_\mu = \partial_\mu \mathbf{R} = h_\mu \hat{e}_\mu$, where h_μ are scale factors. The metric tensor is defined as $\mathcal{G}_{\lambda\mu} = e_\lambda \cdot e_\mu$, and can be written as

$$\mathcal{G}_{\lambda\mu} = \begin{pmatrix} h_s^2 & 0 & 0 \\ 0 & 1 & 0 \\ 0 & 0 & 1 \end{pmatrix}, \quad (2)$$

where $h_s = 1 - n\kappa(s)$. It lowers contravariant indices, while its inverse, denoted $\mathcal{G}^{\lambda\mu}$, raises covariant indices.

For a circular geometry, the curvature is constant $\kappa(s) = \kappa$, and the parametrization can be written as

$$\mathbf{r}(s) = \frac{1}{\kappa} \cos(\kappa s) \hat{e}_x + \frac{1}{\kappa} \sin(\kappa s) \hat{e}_y. \quad (3)$$

The orthogonal curvilinear unit vectors become $\hat{\mathcal{T}}(s) = \partial_s \mathbf{r}(s)$, $\hat{\mathcal{N}}(s) = \partial_s \hat{\mathcal{T}}(s) / |\partial_s \hat{\mathcal{T}}(s)|$ and $\hat{\mathcal{B}}(s) = \hat{\mathcal{T}}(s) \times \hat{\mathcal{N}}(s)$. For the circular parametrization [Eq. (3)] this gives

$$\begin{aligned} \hat{\mathcal{T}}(s) &= -\sin(\kappa s) \hat{e}_x + \cos(\kappa s) \hat{e}_y, \\ \hat{\mathcal{N}}(s) &= -\cos(\kappa s) \hat{e}_x - \sin(\kappa s) \hat{e}_y, \\ \hat{\mathcal{B}}(s) &= \hat{e}_z. \end{aligned} \quad (4)$$

B. Continuum Hamiltonian and strain-induced spin-orbit coupling

The covariant Hamiltonian for describing the motion of electrons in the presence of spin-orbit coupling is

$$\mathcal{H} = -\frac{\hbar^2 \mathcal{G}^{\lambda\mu}}{2m^*} \mathcal{D}_\lambda \mathcal{D}_\mu + \frac{i\hbar}{m^*} \frac{\epsilon^{\lambda\mu\nu}}{\sqrt{G}} \alpha_\lambda \sigma_\mu \mathcal{D}_\nu, \quad (5)$$

where G is the determinant of the metric tensor, \hbar is the reduced Planck constant, m^* is the effective electron mass, α_λ are components of the spin-orbit vector, σ_μ the Pauli vector components, and $\epsilon^{\lambda\mu\nu}$ is the Levi-Civita symbol. We define the covariant spin-orbit field as $\mathcal{A}^\nu = \epsilon^{\lambda\mu\nu} \alpha_\lambda \sigma_\mu / \hbar \sqrt{G}$, which allows us to rewrite the Hamiltonian in Eq. (5) to show a local SU(2) gauge invariance¹⁵⁻¹⁷

$$\mathcal{H} = -\frac{\hbar^2 \mathcal{G}^{\lambda\mu}}{2m^*} (\mathcal{D}_\lambda - i\mathcal{A}_\lambda) (\mathcal{D}_\mu - i\mathcal{A}_\mu). \quad (6)$$

The covariant derivative \mathcal{D}_λ of a covariant vector v_μ is defined as³²

$$\mathcal{D}_\lambda v_\mu = \partial_\lambda v_\mu - \Gamma_{\lambda\mu}^\nu v_\nu. \quad (7)$$

The Christoffel symbols are related to the metric tensor, and are defined as³²

$$\Gamma_{\lambda\mu}^\nu = \frac{1}{2} \mathcal{G}^{\nu\rho} (\partial_\mu \mathcal{G}_{\rho\lambda} + \partial_\lambda \mathcal{G}_{\rho\mu} - \partial_\rho \mathcal{G}_{\lambda\mu}). \quad (8)$$

When curvature is the result of lattice deformation, the associated strain can be defined as the difference in arc length

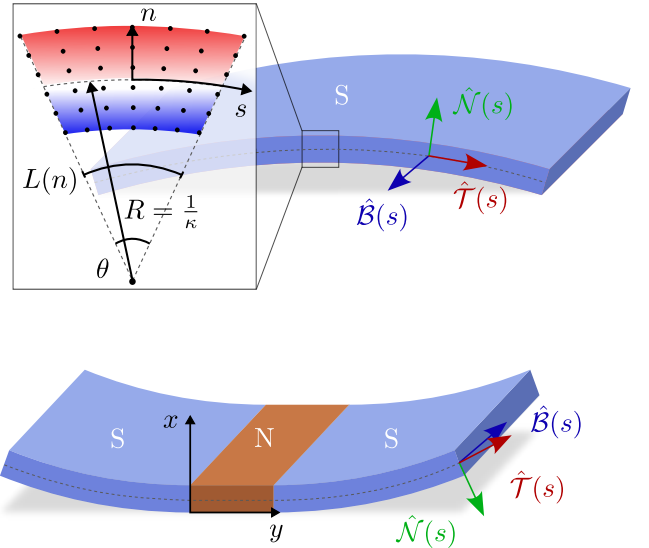


FIG. 1. Thin-film superconductor with bending-strain and an SNS Josephson junction with uniformly curved superconductors and an uncurved normal metal. Curvilinear unit vectors in the tangential $\hat{\mathcal{T}}(s)$, normal $\hat{\mathcal{N}}(s)$, and binormal $\hat{\mathcal{B}}(s)$ direction, as well as the radius of curvature R , are indicated. In the inset, red represents tensile strain and blue indicates compressive strain of the lattice.

between the center $L(0)$ and the outermost layer $L(n)$ normalized by $L(0)$ (see Fig. 1). The arclength is given by $L(n) = \theta(R + n)$, where θ is the subtending angle. Thus, we can write the strain associated with the geometric deformation as^{20,33}

$$\epsilon_{ss} = \frac{\theta(R + n) - \theta R}{\theta R} = \kappa(s)n. \quad (9)$$

This in turn gives rise to an additional potential in the material^{34,35} and, therefore, an electric field $\mathbf{E} \sim \kappa(s)\hat{\mathcal{N}}(s)$ for small strain. An electron moving through this electric field will experience an effective magnetic field $\mathbf{B} \sim \mathbf{p} \times \mathbf{E}$ through the Zeeman interaction in its rest frame. Since the electric field is oriented in the normal direction, it allows us to express the resulting spin-orbit vector as $\boldsymbol{\alpha} = \alpha_N \hat{\mathcal{N}}(s)$, where the coefficient α_N quantifies the strain-induced spin-orbit coupling, being proportional to the local curvature, given by $\alpha_N(s) = a_N \kappa(s)$, with proportionality constant a_N . Thus, the continuum Hamiltonian for a thin film around $n = 0$, can be written as

$$\begin{aligned} \mathcal{H} = & -\frac{\hbar^2}{2m^*} \nabla^2 - \frac{i\hbar^2}{m^*} \sigma_T(s) \alpha_N(s) \partial_b \\ & + \frac{i\hbar^2}{2m^*} \sigma_B [\alpha_N(s) \partial_s + \partial_s \alpha_N(s)], \end{aligned} \quad (10)$$

where $\sigma_T(s) = -\sin[\kappa(s)s] \sigma_x + \cos[\kappa(s)s] \sigma_y$ and $\sigma_B = \sigma_z$, which follows directly from Eq. (4).

C. Discretization and diagonalization

Discretizing the continuum Hamiltonian [Eq. (10)] gives the tight-binding Bogoliubov–de Gennes Hamiltonian:

$$\begin{aligned} \mathcal{H} = & -\sum_{\langle i,j \rangle, \sigma} t_{ij} c_{i,\sigma}^\dagger c_{j,\sigma} - \sum_{i,\sigma} \mu_i c_{i,\sigma}^\dagger c_{i,\sigma} \\ & - \sum_i U_i c_{i,\uparrow}^\dagger c_{i,\uparrow} c_{i,\downarrow}^\dagger c_{i,\downarrow} \\ & - \frac{i}{2} \sum_{\langle i,j \rangle, \sigma, \sigma'} \alpha_N \hat{\mathcal{N}}(s) \cdot (\boldsymbol{\sigma}(s) \times \mathbf{d}_{ij}), \end{aligned} \quad (11)$$

where t is the hopping amplitude, μ_i is the chemical potential, U_i is the local on-site attraction that gives rise to superconductivity. The nearest neighbor vector \mathbf{d}_{ij} points from lattice coordinates $\mathbf{i} = (i_s, i_b)$ to $\mathbf{j} = (j_s, j_b)$, and $\mathbf{d}_{ij} = -\mathbf{d}_{ji}$.

We assume periodic boundary conditions in the binormal direction. Therefore, we Fourier transform the electron creation and annihilation operators,

$$\begin{aligned} c_{i_s, k_b, \sigma} &= \frac{1}{\sqrt{N_b}} \sum_{i_b} c_{i_s, i_b, \sigma} e^{ik_b i_b}, \\ c_{i_s, k_b, \sigma}^\dagger &= \frac{1}{\sqrt{N_b}} \sum_{i_b} c_{i_s, i_b, \sigma}^\dagger e^{-ik_b i_b}, \end{aligned} \quad (12)$$

where N_b represents the total number of lattice sites in the binormal direction. Since the binormal lattice index does not

appear in any of the following expressions, we denote the tangential $i_s \equiv i$ and the binormal momentum $k_b \equiv k$. We choose the Fourier-transformed Nambu \otimes spin space basis

$$\begin{aligned} \hat{B}_{i,k}^\dagger &= \left(c_{i,k,\uparrow}^\dagger \ c_{i,k,\downarrow}^\dagger \ c_{i,-k,\uparrow} \ c_{i,-k,\downarrow} \right), \\ W_k^\dagger &= \left(\hat{B}_{1,k}^\dagger \ \hat{B}_{2,k}^\dagger \ \hat{B}_{3,k}^\dagger \ \dots \ \hat{B}_{N_s,k}^\dagger \right), \end{aligned} \quad (13)$$

which we use to write the Hamiltonian as

$$\mathcal{H} = -\frac{1}{2} \sum_{i,j,k} \hat{B}_{i,k}^\dagger \hat{H}_{i,j,k} \hat{B}_{j,k} = -\frac{1}{2} \sum_k W_k^\dagger H_k W_k, \quad (14)$$

where we have neglected constant shifts to the energy. The site-dependent matrix in the above sum can be written as

$$\begin{aligned} \hat{H}_{i,j,k} = & (2t \cos ka + \mu_i) \delta_{i,j} \tau_3 \otimes \sigma_0 \\ & + t (\delta_{i,j+1} + \delta_{i,j-1}) \tau_3 \otimes \sigma_0 \\ & + \delta_{i,j} (i\Delta_i \tau^+ - i\Delta_i^* \tau^-) \otimes \sigma_y \\ & + \alpha_{ii} \delta_{i,j} \sin ka \hat{\sigma}_T \\ & + \frac{i}{2} \alpha_{ij} (\delta_{i,j+1} - \delta_{i,j-1}) \tau_0 \otimes \sigma_B, \end{aligned} \quad (15)$$

where $\alpha_{ij} = \alpha_N(s_i) + \alpha_N(s_j)$, and $\tau^\pm = \tau_1 \pm i\tau_2$, where the τ matrices are Pauli matrices that operate in Nambu space. Furthermore, the matrix $\hat{\sigma}_T = \text{diag}(\sigma_T, i, \sigma_T^*, i)$, where $\sigma_T(s) = \boldsymbol{\sigma} \cdot \hat{\mathcal{T}}(s)$, and a is the lattice constant.

To diagonalize the Hamiltonian and obtain the eigenenergies we consider the eigenvalue problem $H_k \Phi_{n,k} = \mathcal{E}_{n,k} \Phi_{n,k}$, which has $4N_s$ eigenvalues, where N_s is the total number of lattice sites in the tangential direction. It is equivalent to writing

$$\sum_j \hat{H}_{i,j,k} \hat{\phi}_{j,n,k} = \mathcal{E}_{n,k} \hat{\phi}_{i,n,k}, \quad (16)$$

where

$$\begin{aligned} \hat{\phi}_{i,n,k}^\dagger &= (u_{i,n,k}^*, v_{i,n,k}^*, w_{i,n,k}^*, x_{i,n,k}^*), \\ \Phi_{n,k} &= (\hat{\phi}_{1,n,k}, \hat{\phi}_{2,n,k}, \dots, \hat{\phi}_{N_s,n,k}). \end{aligned} \quad (17)$$

Diagonalizing the $4N_s \times 4N_s$ matrix gives $H_k = P_k D_k P_k^\dagger$, where $P_k = [\Phi_{n,k}]$ is a matrix containing the eigenvalues of H_k . The matrix D_k contains the eigenvalue $\mathcal{E}_{n,k}$ on the n 'th diagonal. Therefore, the total Hamiltonian becomes

$$\mathcal{H} = -\frac{1}{2} \sum_{n,k} \mathcal{E}_{n,k} \gamma_{n,k}^\dagger \gamma_{n,k}, \quad (18)$$

where $\gamma_{n,k}$ is the n 'th element of $\Gamma_k = P_k^\dagger W_k$.

There are pairs of linearly dependent quasiparticle operators $\gamma_{n,k} = \gamma_{n,-k}^\dagger$ that give pairs of identical eigenvalues $\mathcal{E}_{n,k} = -\mathcal{E}_{n,-k}$ with opposite sign. The momentum index lies in the first Brillouin zone $ka \in [-\pi, \pi)$, and for periodic boundary conditions, the values are restricted by $ka = 2\pi m/N_b$, where m is an integer. Thus, we split the momentum

sum into three contributions to obtain a Hamiltonian with only linearly independent quasiparticle operators³⁶:

$$\mathcal{H} = - \sum_{n,0 < ka < \pi} \mathcal{E}_{n,k} \gamma_{n,k}^\dagger \gamma_{n,k} - \sum_{\mathcal{E}_n \geq 0} (\mathcal{E}_{n,0} \gamma_{n,0}^\dagger \gamma_{n,0} + \mathcal{E}_{n,\pi} \gamma_{n,\pi}^\dagger \gamma_{n,\pi}). \quad (19)$$

For zero momentum and $ka = \pi$ we used the following relations for the pairs of energy eigenvalues: $\mathcal{E}_{n,0} = -\mathcal{E}_{n+2N_s,0}$ and $\mathcal{E}_{n,\pi} = -\mathcal{E}_{n+2N_s,\pi}$. All expectation values are expressed similarly, so we define a new sum

$$\sum' = \sum_{n,k} + \sum_{n,0 < ka < \pi} + \sum_{\mathcal{E}_n \geq 0, ka = \pi}. \quad (20)$$

The old fermion operators can now be expressed using the new quasiparticle operators:

$$c_{i,k,\uparrow} = \sum_n u_{i,n,k} \gamma_{n,k}, \quad c_{i,k,\downarrow} = \sum_n v_{i,n,k} \gamma_{n,k}, \quad (21)$$

$$c_{i,-k,\uparrow}^\dagger = \sum_n w_{i,n,k} \gamma_{n,k}, \quad c_{i,-k,\downarrow}^\dagger = \sum_n x_{i,n,k} \gamma_{n,k},$$

which are useful in extracting numerical estimates for observables of interest.

D. Order parameters and observables

To compare different symmetries, we define the superconducting order parameters as $\Delta_i(\tau) = \langle \mathcal{T} c_{i,\sigma}(\tau) c_{i',\sigma'}(0) \rangle$, where \mathcal{T} is the time ordering operator, and τ is the relative time coordinate scaled by \hbar/t . Thus, we can investigate the order parameters of even- ($\tau = 0$) and odd-frequency ($\tau \neq 0$) correlations. In Table I, we introduce the notation for the relevant combinations of underlying Spin-Parity-Orbital-Time (SPOT) symmetries that ensure overall odd order parameter symmetry³⁷.

	<i>S</i>	<i>P</i> *	<i>O</i>	<i>T</i> *	
\mathcal{S}_0	-1	1	1	1	even-frequency <i>s</i> -wave singlet
$\mathcal{S}_{\sigma\sigma'}(\tau)$	1	1	1	-1	odd-frequency <i>s</i> -wave triplets
$\mathcal{P}_{\sigma\sigma'}^m$	1	-1	1	1	even-frequency <i>p</i> ^{<i>m</i>} -wave triplets
$\mathcal{P}_0^m(\tau)$	-1	-1	1	-1	odd-frequency <i>p</i> ^{<i>m</i>} -wave singlet

TABLE I. Spin-parity-orbital-time symmetries of order parameters defined in the main text. The operators T^* and P^* are denoted with an asterisk as they only commute the relative coordinates of the electron operators and do not invert the full spaces.

Adhering to the symmetry relations summarized in Table I, we can define the *s*- and *p*-wave singlet and triplet amplitudes as

$$\mathcal{S}_{i,0} = \frac{1}{2} [\langle c_{i,\uparrow} c_{i,\downarrow} \rangle - \langle c_{i,\downarrow} c_{i,\uparrow} \rangle], \quad (22)$$

$$\mathcal{S}_{i,\uparrow\downarrow}(\tau) = \frac{1}{2} [\langle c_{i,\uparrow}(\tau) c_{i,\downarrow}(0) \rangle + \langle c_{i,\downarrow}(\tau) c_{i,\uparrow}(0) \rangle], \quad (23)$$

$$\mathcal{P}_{i,0}^m(\tau) = \sum_{\pm} \pm \frac{1}{2} [\langle c_{i,\uparrow}(\tau) c_{i\pm m,\downarrow}(0) \rangle - \langle c_{i,\downarrow}(\tau) c_{i\pm m,\uparrow}(0) \rangle], \quad (24)$$

$$\mathcal{P}_{i,\uparrow\downarrow}^m = \sum_{\pm} \pm \frac{1}{2} [\langle c_{i,\uparrow} c_{i\pm m,\downarrow} \rangle + \langle c_{i,\downarrow} c_{i\pm m,\uparrow} \rangle], \quad (25)$$

$$\mathcal{P}_{i,\sigma\sigma}^m = \sum_{\pm} \pm \langle c_{i,\sigma} c_{i\pm m,\sigma} \rangle. \quad (26)$$

Here m is one lattice spacing in either the tangential or binormal direction, and the time-dependent operators are given by $c_{i,\sigma}(\tau) = e^{i\mathcal{H}\tau} c_{i,\sigma} e^{-i\mathcal{H}\tau}$. Observe here that the *p*-wave correlations have $i - i' \neq 0$, and the *s*-wave correlations have $i - i' = 0$.

The gap equation in the mean-field approximation is given by $\Delta_i = U_i \mathcal{S}_{i,0}$, which in the new quasiparticle basis yields

$$\Delta_i = \frac{U_i}{2N_b} \sum'_{n,k} [x_{i,n,k}^* u_{i,n,k} - w_{i,n,k}^* v_{i,n,k}] \tanh(\beta \mathcal{E}_{n,k}), \quad (27)$$

where we have used that $\langle \gamma_{n,k}^\dagger \gamma_{n',k} \rangle = f(2\mathcal{E}_{n,k}) \delta_{n,n'}$ and $f(2\mathcal{E}_{n,k})$ is the Fermi-Dirac distribution, and β is the inverse temperature. The corresponding expressions for Eq. (22)-(26) in the quasiparticle basis of Eq. (21) that are used for computation are given in Appendix A for convenience.

We can consider the derivatives of the odd-frequency order parameters to eliminate the dependence on the relative time coordinate. The odd-frequency order parameters are odd in time and vanish at $\tau = 0$, while their derivatives are even and typically finite when evaluated at this point³⁸. Therefore, we will evaluate all correlations at $\tau = 0$. The relative time derivative is defined as $\hat{\Delta}_i(\tau) = \langle \mathcal{T} \frac{\partial c_{i,\sigma}(\tau)}{\partial \tau} c_{i',\sigma'}(0) \rangle$, where the derivative is computed by commuting the electron operator with the Hamiltonian,

$$\frac{\partial c_{i,\sigma}(\tau)}{\partial \tau} = i [\mathcal{H}, c_{i,\sigma}(\tau)]. \quad (28)$$

To find the spin-current, one can consider continuity equations. Using the Heisenberg equation of motion to rewrite the time derivative, the continuity equation for the spin-current can be expressed as

$$\sum_m \mathbf{J}_{i,m} = -i [\mathcal{H}, \mathbf{S}_i]. \quad (29)$$

Here, \mathcal{H} is the Hamiltonian and m enumerates the surface normals of the unit cell i . By comparing the current flowing in and out from a single unit cell in the tangential direction, a final expression can be obtained³⁹. Thus, \mathbf{J} denotes the spin-current flowing parallel to $\hat{\mathcal{T}}$ in real space, with components in spin space J^μ , where $\mu = (s, n, b)$ indicates spin alignment in the tangential, normal, and binormal directions. The components of the spin-current \mathbf{J} are only conserved in areas without spin-orbit coupling. We will therefore only examine spin-current as a useful observable in cases where the material is not curved at i , and $\alpha_N \neq 0$, i.e. in an uncurved normal metal sandwiched between two curved superconductors, as in Fig. 1. By using the quasiparticle operators and elements defined in Eq. (17), we find the tangential- and binormal-components of the spin-current

$$J_i^s = \frac{-2t}{N_b} \sum_{n,k,\pm} \pm \Re \left\{ (v_{i\pm 1,n,k}^* u_{i,n,k} - u_{i\pm 1,n,k}^* v_{i,n,k}) f(2\mathcal{E}_{n,k}) - (x_{i\pm 1,n,k}^* w_{i,n,k} - w_{i\pm 1,n,k}^* x_{i,n,k}) f(-2\mathcal{E}_{n,k}) \right\}, \quad (30)$$

$$J_i^b = \frac{-2t}{N_b} \sum_{n,k,\pm} \pm \Im \left\{ (u_{i\pm 1,n,k}^* u_{i,n,k} - v_{i\pm 1,n,k}^* v_{i,n,k}) f(2\mathcal{E}_{n,k}) - (w_{i\pm 1,n,k}^* w_{i,n,k} - x_{i\pm 1,n,k}^* x_{i,n,k}) f(-2\mathcal{E}_{n,k}) \right\}. \quad (31)$$

The spin magnetization is defined as $\mathbf{S}_i = \langle c_{i,\alpha}^\dagger \boldsymbol{\sigma}^{\alpha\beta} c_{i,\beta} \rangle$, which means that the binormal component becomes

$$S_i^b = \frac{2}{N_b} \sum_{n,k} \left[(|u_{i,n,k}|^2 - |v_{i,n,k}|^2) f(2\mathcal{E}_{n,k}) + (|w_{i,n,k}|^2 - |x_{i,n,k}|^2) f(-2\mathcal{E}_{n,k}) \right]. \quad (32)$$

Having defined the order parameters and observables of interest, we can now examine their variation with increasing, uniform strain.

III. RESULTS

We examine the effects of bending-strain in clean, conventional superconducting films in Section III A. In Section III B, we consider the additional effect of proximity-coupling the strained superconductor to a normal metal, and in Section III C we consider the proximity-induced effects in SNS junctions.

In the following, we normalize the curvature to the superconducting coherence length $\alpha_N = \kappa\xi$, with proportionality constant $a_N = 1$. This can be used to relate the effective spin-orbit strength to the strain via $\alpha_N = \epsilon_{ss}\xi/n$, where $n = (N_n - 1)a/2$ is the length from the center of the film to the outermost layer (see Fig. 1), and a is the lattice spacing. Using this, any specific strain values indicated from now on will refer to the strain at the upper/lower plane of the superconductor. For illustrative purposes, we select parameters corresponding to superconducting niobium, with $\alpha_N = 2.3\epsilon_{ss}/(N_n - 1)$, where ϵ_{ss} is the strain in percent. The choice of material is arbitrary, chosen here to provide a familiar scale in comparison with purely spin-orbit-coupled systems, and the results presented here will apply to any conventional thin-film superconductor⁴⁰⁻⁴³. We examine film thicknesses $N_n \in (3, 6, 9)$, and set $\xi/a = 2.3$ so that α_N falls within the common range for SOC-systems. We denote the *total* number of lattice sites in the tangential, normal, and binormal direction with N_s, N_b , and N_b , respectively. The number of lattice sites in the tangential direction in the superconductors and normal metal *individually* will be denoted N_S and N_N respectively, as indicated in Fig. 2. The thin-film Hamiltonian is solved by summing over one-dimensional chains with a binormal momentum index k and averaging over the first Brillouin zone, as described in Eqs. (14) and (20). Strain and curvature are incorporated as spin-orbit coupling, with the Pauli matrices rotating according to Eq. (4). The coordinate system is oriented such

that the normal metal, when present, lies in the $y - z$ plane, as illustrated in Fig. 1.

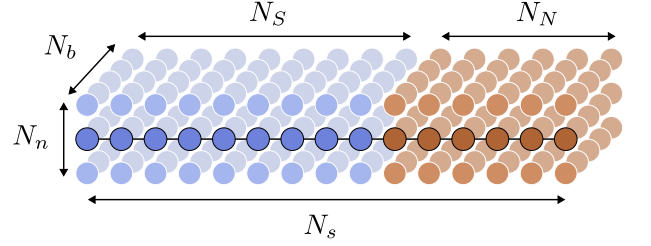


FIG. 2. The illustration shows the dimensions used in the numerical treatment of an SN bilayer. Assuming periodic boundary conditions in the binormal direction, the thin-film is modeled as a one-dimensional chain. The thickness (N_n) provides an effective SOC, specifically in the direction normal to the strained superconductor.

A. Bending-strain in a thin-film superconductor

We initialize a superconductor with an s-wave gap on a square lattice, which is solved self-consistently with an iterative diagonalization by updating the gap equation (15) with the expression in Eq. (27) until their absolute difference falls below a threshold, here set to 10^{-6} . We set the number of sites in the binormal and tangential direction to be square, with $N_b = N_s = 99$ in this subsection. By selecting an odd number of lattice sites, the end of the Brillouin zone does not contribute, i.e. we can ignore the last term in Eq. (20), since $ka = 2\pi m/N_b$, where m is an integer. While a specific number is chosen for illustration, the results are not sensitive to the number of lattice sites and remain consistent across different configurations, although a more sophisticated model would be expected to show atomic-scale oscillation of the strength of the superconductivity^{41,43}. Furthermore, normalizing to the hopping t , we set the attractive potential parameter to $U = 1.5$, the chemical potential to $\mu = 1$, and the temperature to $T = 0.2$.

The direction of asymmetry of the strain-induced spin-orbit coupling in the superconductor is in $\hat{N}(s)$, which creates a mixed parity s- and p-wave order parameter in the superconductor. The magnitude of the s-wave gap will diminish as a function of the strain, as shown in Fig. 3. This is analogous to doing self-consistency calculations for an increasing Rashba coefficient in a spin-orbit coupled superconductor, which yields the same results²⁷.

We denote the p-wave triplet pairings with no spin projection as $\mathcal{P}_{\uparrow\downarrow}^s$, and the spin-polarized triplets as \mathcal{P}_{σ}^b , as in-

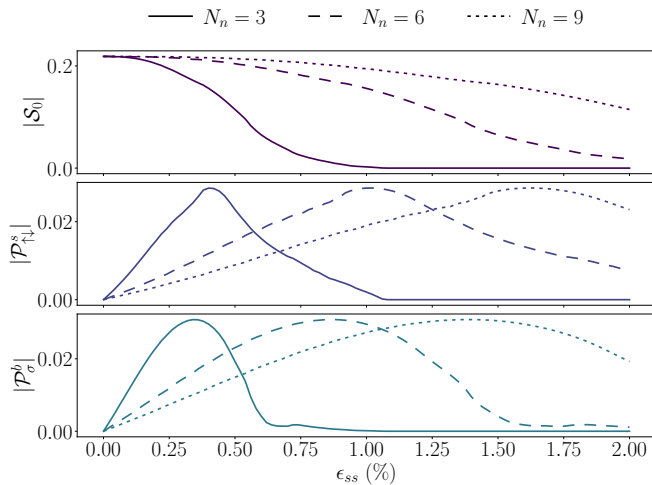


FIG. 3. The even-frequency s-wave singlet and p-wave triplet pairings at the center of the superconductor as a function of the strain ϵ_{ss} . The spin-polarized p-wave amplitudes are equal in magnitude $|\mathcal{P}_\sigma^b| = |\mathcal{P}_{-\sigma}^b|$. Parameters are given in the main text.

indicated in Table I. With time-inversion symmetry conserved, the spin-polarized p-wave amplitudes are equal in magnitude $|\mathcal{P}_\uparrow^b| = |\mathcal{P}_\downarrow^b|$. The superconducting gap closes completely for high enough strain, so that both s- and p-wave correlations become negligible. The thicker the film, the higher strain it can support while maintaining superconductivity. The curvature at a given strain is less for thicker films, and so the effective SOC is weaker. The singlet s-wave and finite triplet p-wave order pairings are shown in Fig. 3 as a function of the strain. The pairings arise through the entire superconductor because the superconductor has uniform circular curvature, giving a constant bending-strain profile and equivalent SOC-strength. If the strain is only applied to a certain part, the p-wave amplitudes will only be finite locally. For instance, in an ellipse, the correlations are localized at the apexes⁴⁴.

B. SN bilayer with bending-strain in S

Next, we consider a superconductor-normal metal (SN) bilayer, with an example of arbitrarily chosen length of superconductor with $N_S = 50$ sites, a normal metal with $N_N = 21$ sites, and $N_b = 71$ sites in the binormal direction. The odd number here again simplifies the sum in Eq. (20), as the end of the Brillouin zone does not contribute, as in Section III A. The film thickness in the normal direction is in this case set to $N_n = 3$, and the strain is only applied to the superconductor.

Without curvature, the interface between the conventional, even-frequency s-wave spin-singlet (finite S_0) superconductor and a normal metal breaks translational symmetry, which will create odd-frequency p-wave singlets $[\mathcal{P}_0^s(\tau)]$ ²⁶. These p-wave singlets are dependent only on Andreev reflections⁴⁵. The addition of bending-strain will then reduce the gap within the superconductor and create an order parameter with an even frequency mixed parity $\mathcal{S}_0 + \mathcal{P}_{\uparrow\downarrow}^s$ and \mathcal{P}_σ^b , as seen in Fig. 3, which now penetrates into the normal metal through the

proximity effect.

In Fig. 4, we show the even-frequency pairing amplitudes and the relative time derivatives of the finite odd-frequency pairings at the interface. The even-frequency amplitudes originate from the bending-strain via the spin-asymmetry introduced by the effective spin-orbit coupling in the superconductor, while the interface between the materials induces the odd-frequency pairings. The even-frequency p-wave triplets $\mathcal{P}_{\uparrow\downarrow}^s$ persist throughout the bulk, and these triplets have an interface-dependence on both Andreev and normal reflections⁴⁵. They vanish for $\alpha_N = 0$, in contrast to $\mathcal{P}_0^s(\tau)$, which remains finite, as can be seen in Fig. 4. Furthermore, since the superconductors are strained and the normal metal is not, the bending-induced spin-orbit coupling vanishes at the interfaces. This interfacial change acts on spins like a local spin splitting in the binormal direction, giving rise to an odd-frequency $\mathcal{S}_{\uparrow\downarrow}(\tau)$ -wave triplet and $\mathcal{P}_0^b(\tau)$ -wave singlet contribution.

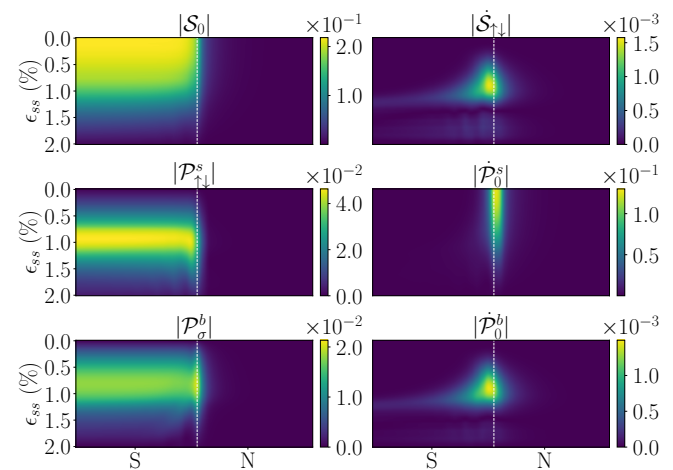


FIG. 4. The pairing amplitudes around the SN interface for increasing strain in the superconductor. The first column shows the non-zero even-frequency pairings and the second column is the relative time derivative of the odd-frequency pairings at $\tau = 0$. The spin-polarized p-wave pairings are equal in magnitude $|\mathcal{P}_\sigma^b| = |\mathcal{P}_{-\sigma}^b|$. The derivatives are compared to the amplitudes of the corresponding odd-frequency pairings in Fig. B.1. System parameters are given in the main text.

By considering the mechanisms for interconversion between the different symmetries of the superconducting correlations, we can therefore detangle the independent contributions generated by the interface and the strain. By examining Fig. 4, we can see how their respective magnitudes can be tuned with the strain ϵ_{ss} , for which a number of external control mechanisms exist, for example mechanical or thermoelectric manipulation, voltage-control from piezoelectric actuators⁸, or light-control via a photostrictive substrate⁴⁶.

For completeness, we compare the derivatives in Fig. 4 with the magnitudes of the corresponding odd-frequency pairings in Fig. B.1 in the Appendix. There we see that the amplitudes – which remain within the same order for relative times within that order – are comparable to the derivative evaluated at relative time $\tau = 0$.

C. SNS junction with bending-strain in S

Lastly, we consider an SNS junction with strained superconductors and an un-strained, uncurved normal metal, as illustrated in Fig. 1. A charge-current flows across the normal metal when there is a phase difference between the superconductors^{47,48}. In addition to the charge current, we find that a spin-current flows across the junction whenever there is bending-strain in the superconductors. Spin current is in general not a conserved quantity since SOC prevents spin from being a good quantum number⁴⁹. However, in our model there is no strain or SOC within the normal metal, and so any spin-current is therefore conserved in this region.

In Fig. 5, we show the tangential and binormal components of the spin current \mathbf{J} at the center of the normal metal. The sign of J^b depends on the length of the normal metal and strain, resulting in so-called $0 - \pi$ oscillations as a function of both length and the effective spin-orbit coupling strength experienced, shown here as a function of the bending-strain in the superconductor. The $0 - \pi$ oscillations in J^b as a function of length are included in Appendix C for completeness. Changes in current-direction as indicated by $0 - \pi$ oscillations are well known in Josephson junctions with a ferromagnetic weak link⁵⁰⁻⁵², but in SNS junctions they are so-far only found when there exists a non-equilibrium electron distribution in N⁵³. This result therefore indicates that, with regards to generating a Josephson current, strain, or effective SOC, acts on the normal metal in a similar way to a Zeeman interaction in a ferromagnet. A subgap spin Josephson effect has also been suggested in the topologically nontrivial phase of topological Josephson junctions with a magnetic field and SOC in the superconductors⁵⁴, and a superconducting diode effect has been noted due to a combination of SOC and magnetic field or intrinsically p-wave superconductors⁵⁵. In our case, we show that this current can appear when using conventional s-wave superconductors with bending-strain and a simple normal metal weak link.

At low strain, we see in Fig. 5 that the dominant Josephson-current is carried by spins polarized in the tangential direction, while J^b takes precedence after the $0 - \pi$ transition of J^s , due to the increasing spin-orbit coupling. The sinusoidal current-phase relation of J^s is shown in the inset of Fig. 5. The binormal component of the spin current consists of a constant value plus a cosine term. Therefore, it is possible to create a small, *pure* spin-current $\mathbf{J} = J^b \hat{\mathcal{B}}(s)$ flowing through the junction. It has been shown that the proportion of spin current in ferromagnetic Josephson junctions can be tuned by the phase difference⁵⁶. Here, it is remarkable to note both that a spin current can be *induced solely* from applied strain in a conventional SNS Josephson-junction, and further that the direction of this current can be *tuned* by the magnitude of this applied strain.

In Fig. 6, we show the spin-current J^s again, this time as a function of both strain and position in N , alongside the induced spin-magnetization S^b . A combination of SOC and charge current in normal metals generically leads to spin accumulation⁵⁷; the charge current shifts the Fermi contour along the k_s -axis in momentum space, which, in the presence of SOC, creates a finite spin magnetization in the binormal direction. The ap-

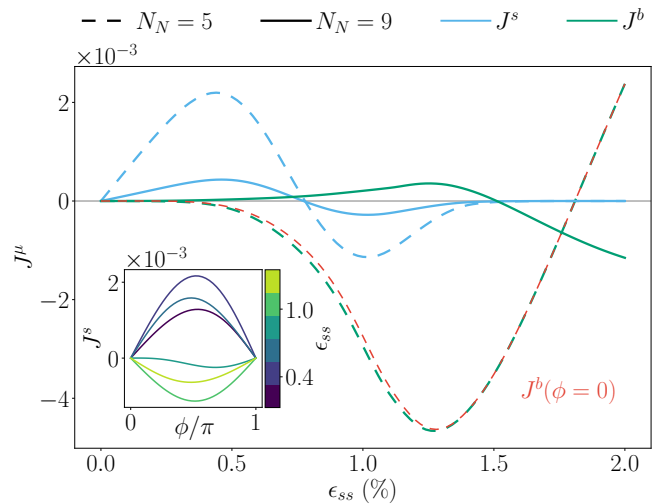


FIG. 5. The nonzero spin-current components at the center of the normal metal for two different lengths $N_N = (5, 9)$ at phase difference $\phi = \pi/2$. We have used $N_S = 50$ sites in the superconductors and $N_b = 2N_S + N_N$ in both cases. The remaining parameters are identical to the main text. J^b for $N_N = 5$ at zero phase difference $\phi = 0$ is shown in red. The inset shows the sinusoidal form of J^s , with a change in sign as a function of strain.

pearance of a spin magnetization ϵ_{ss} can therefore be attributed to the Edelstein effect⁵⁸. Since we have fixed the phases in the superconductors, the spin accumulation is strongest within the normal metal, as seen in Fig. 6. In our numerical scheme, we split the phase difference equally between the two superconductors. The diagonalization gives proximity-induced pairings in the normal metal, with a phase gradient $\partial_s \phi$ in the tangential direction. When this phase gradient is nonzero, a charge current will flow. This gradient diminishes away from the interfaces within the superconductors, so the spin magnetization [S^b] and charge current will eventually decay there.

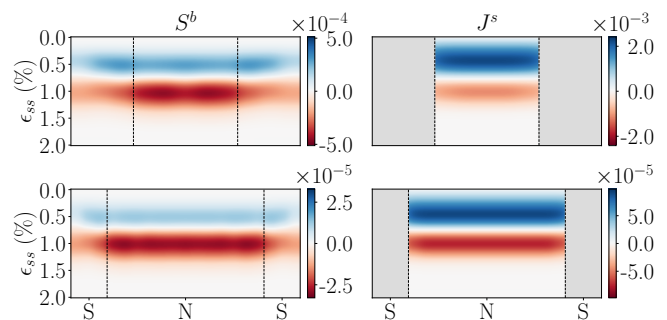


FIG. 6. The spin-magnetization S^b and spin-current component J^s within the normal metal, for phase difference $\phi = \pi/2$ between the superconductors. The first row has $N_N = 5$ and the second row $N_N = 13$. We have used $N_S = 50$ and $N_b = N_s$, while the rest of the parameters are identical to the main text.

We see from Fig. 6 that the switch in magnetization can be determined from the $0 - \pi$ switching profile of J^s . The principal reason why no magnetic field or intrinsic p-wave order is

required in this case is due to the combination of effective-SOC and interfacial effects on rotating the proximity-induced correlations, and is inherently linked to the thin-film nature of the system, which retains an additional term in the cross-product of Eq. (11) compared with the one-dimensional analysis of most triplet transport analysis to date. When considering two dimensions, we get a $\sigma_T k_s$ -term in the sb -plane in the presence of a phase gradient. This creates spin-polarized triplets that can engender a magnetization in the binormal direction, and plays the role typically provided by a magnetic field. We therefore see that strain can be an effective generator and controller/switcher of spin-current and magnetization in SNS junctions.

IV. DISCUSSION AND CONCLUSION

We have considered the effect of bending-strain in thin films of clean, conventional, s-wave superconductors, and its proximity-induced effects on the symmetries of the superconducting correlations persisting in SN and SNS heterostructures. In the strained superconductor alone, we find that the strain reduces the s-wave gap while increasing even-frequency p-wave triplets both with and without spin polarization throughout the superconductor. Including a normal-metal interface leads to the additional generation of odd-frequency pairings – odd-frequency $\mathcal{P}_0^s(\tau)$ from the interface alone, and a contribution to $\mathcal{S}_{\uparrow\downarrow}(\tau)$ -wave triplet and $\mathcal{P}_0^b(\tau)$ -wave singlet from both the interface and strain – and their magnitudes can be tuned by the strain. Using these principles, we find that the strain alone can induce a spin-current in SNS junctions, and tuning the strain can switch the current direction. The presence of a spin-polarized current results in a strain-switchable magnetization in the normal metal, and we show that this pure spin current can be generated in the junction without a magnetic field, and even when the phase difference in the junction is $\phi = (0, \pi)$. Considering the many control mechanisms for nanomechanical strain, this may find several uses in superconducting spintronics and quantum logic circuits, from control of superconducting qubits to controllable memories⁵².

We showed in Section III A that bending-strain in an isolated superconducting film induces p-wave triplet pairings throughout the superconductor for uniform curvature. Their magnitude is always around one order lower than the s-wave singlet, and die out as the parent correlation diminishes. Since the superconducting order parameter started out fully s-wave singlet, our self-consistency calculations included only the s-wave gap. We expect that if the p-wave correlations are included in the self-consistency requirement, p-wave pairings may stabilize to form the majority pairing population for increasingly high strain. For non-constant curvatures in the film, the gap would reduce locally in areas with high strain, and the p-wave contribution would increase only locally. We would also expect the sign of the curvature in each arm of the SNS junction to affect the ground state⁶. For an S-shaped junction with opposite but equal curvatures in each arm, we would expect the spin magnetization to become vanishingly small as the spin polarization contributions from each interface would cancel⁶.

In this article we have shown the effects of bending-strain

magnitudes of up to 2%, with all the major effects we report generally achievable with $\epsilon_{ss} < 1\%$. We have shown how thicker materials can support superconductivity at higher strains, but since materials typically become very brittle at cryogenic temperatures, it is prudent to limit strain to around 1%. In addition, while a number of techniques are being developed for designing curvilinear superconductors in three dimensions²⁴, most devices for dynamically imparting strain in-situ, such as piezoelectric actuators^{8,59} are currently restricted to this same order.

Bending-strain translates into an effective SOC with symmetry breaking axis in the radial direction. Since the arc length defining the radius of curvature changes for every layer in the film, the total bending-strain of any one sample depends on the film thickness according to Eq. (9). We showed results for thicknesses $N_n = (3, 6, 9)$, and for equal strains these thicknesses have both a different curvature and a different corresponding effective SOC. We provide an overview of their comparative values in Table C.1, where we for convenience also compare the SOC energy with respect to the superconducting gap. When combining the radial bending-strain with interfacial-Rashba SOC in thin-film heterostructures, these two different symmetry-breaking axes combine to give a nuanced mixture of odd- and even-frequency correlations. They can be harnessed in conjunction with the spontaneous charge current that exists in an SNS Josephson junction, giving pure spin-current even at zero phase difference in the junction. The spin current can drive a switchable magnetization in the normal metal. Strain alone may therefore also induce a superconducting diode effect⁵⁵.

In our approach, we have assumed that the imparted strain is sufficiently small to not significantly affect the electron-phonon interaction. However, to the best of our knowledge there is as yet no clear experimental data indicating for what strains this assumption breaks down. For larger strains, we would expect a significant modification of the electron bands due to lattice deformation, and a shift in the electron-phonon interaction between compressive and tensile regions. It would be instructive to further explore the nature of this change in the interaction in highly strained superconductors in the future.

In further development of this setup, it would be possible to include intrinsic Dresselhaus SOC in the normal metal, as well as out-of-plane symmetry breaking Rashba SOC induced via a substrate. Furthermore, since the normal metal undergoes no in-situ deformation, it would also be possible to include extrinsic Rashba SOC from gating, giving an additional control over the interconversion mechanisms for the superconducting correlations. While we also restricted the analysis in this study to conventional superconductors, a natural extension would be to consider unconventional materials, or multiband superconductors. In those cases modifications to the electron-phonon interaction may play an even bigger role, and strain-deformation of the bands in two-band superconductors could have profound implications for stabilizing superconductivity at high magnetic fields⁶⁰.

ACKNOWLEDGMENTS

We acknowledge funding via the ‘‘Outstanding Academic Fellows’’ programme at NTNU and the Research Council of Norway Grant Nos. 302315 and 262633.

Appendix A: Pair amplitudes

The pairing amplitudes can be found by inserting the operators in Eq. (21) into (22)-(26). This gives the following expressions for the even- and odd-frequency s- and p-wave singlet and triplet amplitudes, and their derivatives

$$\mathcal{S}_{0,i} = \frac{1}{2N_b} \sum'_{n,k} \left[x_{i,n,k}^* u_{i,n,k} - w_{i,n,k}^* v_{i,n,k} \right] \tanh(\beta \mathcal{E}_{n,k}), \quad (\text{A1})$$

$$\mathcal{S}_{i,\uparrow\downarrow}(\tau) = \frac{1}{2N_b} \sum'_{n,k} (x_{i,n,k}^* u_{i,n,k} + w_{i,n,k}^* v_{i,n,k}) (f(2\mathcal{E}_{n,k}) e^{2i\mathcal{E}_{n,k}\tau} + f(-2\mathcal{E}_{n,k}) e^{-2i\mathcal{E}_{n,k}\tau}), \quad (\text{A2})$$

$$\dot{\mathcal{S}}_{i,\uparrow\downarrow}(\tau=0) = \frac{-i}{N_b} \sum'_{n,k} \mathcal{E}_{n,k} (x_{i,n,k}^* u_{i,n,k} + w_{i,n,k}^* v_{i,n,k}) \tanh(\beta \mathcal{E}_{n,k}), \quad (\text{A3})$$

$$\begin{aligned} \mathcal{P}_{i,0}^s(\tau) = \frac{1}{2N_b} \sum'_{\pm,n,k} \pm \left[(x_{i\pm 1,n,k}^* u_{i,n,k} - w_{i\pm 1,n,k}^* v_{i,n,k}) f(-2\mathcal{E}_{n,k}) e^{-2i\mathcal{E}_{n,k}\tau} \right. \\ \left. + (w_{i,n,k}^* v_{i\pm 1,n,k} - x_{i,n,k}^* u_{i\pm 1,n,k}) f(2\mathcal{E}_{n,k}) e^{2i\mathcal{E}_{n,k}\tau} \right], \end{aligned} \quad (\text{A4})$$

$$\begin{aligned} \dot{\mathcal{P}}_{i,0}^s(\tau=0) = \frac{-i}{N_b} \sum'_{\pm,n,k} \pm \mathcal{E}_{n,k} \left[(x_{i\pm 1,n,k}^* u_{i,n,k} - w_{i\pm 1,n,k}^* v_{i,n,k}) f(-2\mathcal{E}_{n,k}) \right. \\ \left. + (x_{i,n,k}^* u_{i\pm 1,n,k} - w_{i,n,k}^* v_{i\pm 1,n,k}) f(2\mathcal{E}_{n,k}) \right], \end{aligned} \quad (\text{A5})$$

$$\mathcal{P}_{i,0}^b(\tau) = \frac{-i}{N_b} \sum'_{n,k} \sin(ka) (x_{i,n,k}^* u_{i,n,k} + w_{i,n,k}^* v_{i,n,k}) (f(2\mathcal{E}_{n,k}) e^{2i\mathcal{E}_{n,k}\tau} + f(-2\mathcal{E}_{n,k}) e^{-2i\mathcal{E}_{n,k}\tau}), \quad (\text{A6})$$

$$\dot{\mathcal{P}}_{i,0}^b(\tau=0) = \frac{-1}{N_b} \sum'_{n,k} \mathcal{E}_{n,k} \sin(ka) (x_{i,n,k}^* u_{i,n,k} + w_{i,n,k}^* v_{i,n,k}) \tanh(\beta \mathcal{E}_{n,k}), \quad (\text{A7})$$

$$\begin{aligned} \mathcal{P}_{i,\uparrow\downarrow}^s = \frac{1}{2N_b} \sum'_{n,k,\pm} \pm \left[(x_{i\pm 1,n,k}^* u_{i,n,k} + w_{i\pm 1,n,k}^* v_{i,n,k}) f(-2\mathcal{E}_{n,k}) \right. \\ \left. + (x_{i,n,k}^* u_{i\pm 1,n,k} + w_{i,n,k}^* v_{i\pm 1,n,k}) f(2\mathcal{E}_{n,k}) \right], \end{aligned} \quad (\text{A8})$$

$$\mathcal{P}_{i,\uparrow\uparrow}^b = \frac{-2i}{N_b} \sum'_{n,k} w_{i,n,k}^* u_{i,n,k} \sin(ka) \tanh(\beta \mathcal{E}_{n,k}), \quad (\text{A9})$$

$$\mathcal{P}_{i,\downarrow\downarrow}^b = \frac{-2i}{N_b} \sum'_{n,k} x_{i,n,k}^* v_{i,n,k} \sin(ka) \tanh(\beta \mathcal{E}_{n,k}). \quad (\text{A10})$$

Appendix B: Odd-frequency amplitudes

The odd-frequency order parameters are influenced by the relative time coordinate τ , which is scaled by \hbar/t and may appear arbitrary. We have found that the amplitudes remain within the same order of magnitude for relative times that

are within the same order. They are also comparable to the derivative evaluated at zero. In Fig. B.1, we have plotted the order parameters at $\tau = 1$, along with their derivatives evaluated at $\tau = 0$.

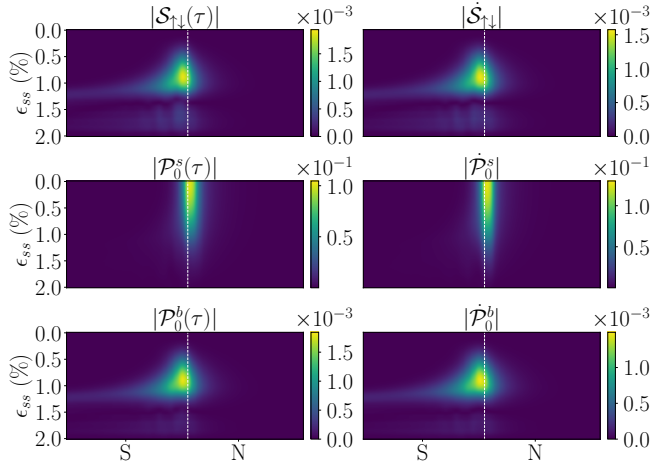


FIG. B.1. The odd-frequency order parameters that are finite at the superconductor-normal metal interface along with their relative time derivatives. The first column is evaluated at $\tau = 1$, and their derivatives in the second column at $\tau = 0$.

Appendix C: Spin-current $0 - \pi$ oscillations with length

In an SNS junction, the binormal component of the spin-current in the tangential direction, J^b , undergoes $0 - \pi$ oscillations as a function of both the applied strain to the superconductors, as seen in Fig. 5, and as a function of the length of the normal metal N_N . These $0 - \pi$ -transitions as a function of length are shown in Fig. C.2, where the transition in strain can also be seen for $N_N = 3, 6$. Further changes in sign occur at other lengths for higher strain (see Fig. 5).

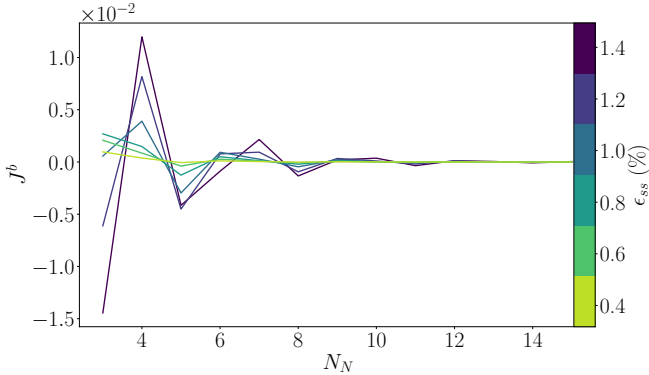


FIG. C.2. The binormal component of the spin-current exhibits $0 - \pi$ oscillations as a function of increasing number of lattice sites in the normal metal, N_N . The values are taken from the center of the normal metal. We have used $N_S = 40$, $N_b = 99$, and $N_n = 3$ sites.

Appendix D: Comparison of curvatures, strain and SOC-energy

We take the strain-induced SOC⁵ $\alpha_N = a_N \kappa$ to be of the order $\alpha_N \approx \kappa$. For specificity, we consider a BCC lattice Niobium film with $a = 1.65 \text{ \AA}^{61}$, $m^* = 2.14 m_e$, $|k_F| = 1.18 \text{ \AA}^{-1}$,⁶² and the gap $|\Delta| = 2.32 \text{ meV}^{63}$. In Table C.1, we then compare the SOC energy $\Delta_{\text{soc}} = \hbar^2 \kappa |k_F| / m^*$ with the gap for different values of strain, and show how this relates to the geometric curvature $\kappa = 1/R$, where R is the radius of curvature, for three different film thicknesses, $N_n = (3, 6, 9)$. Note that since the SOC strength scales with the curvature, and the strain scales with the curvature and thickness, the effective SOC strength scales with strain and the inverse of the thickness. This is apparent in the Fig. 3, where we see a shift along strain-axis for increasing N_n .

N_n	$\kappa \text{ (nm}^{-1}\text{)}$	$\epsilon_{ss} \text{ (\%)}$	$\Delta_{\text{soc}}/\Delta$
3	0.061	1	10.70
	0.121	2	21.40
	0.182	3	32.10
6	0.024	1	4.28
	0.048	2	8.56
	0.073	3	12.84
9	0.015	1	2.67
	0.030	2	5.35
	0.045	3	8.02

TABLE C.1. In the table above are different thicknesses of Niobium (N_n layers). We give the curvature κ and the resulting strain ϵ_{ss} (%). In the last column we compare the SOC energy Δ_{soc} with the superconducting gap Δ .

* Corresponding author: sol.jacobsen@ntnu.no

¹ K. Kaiho, T. S. Luhman, M. Suenaga, and W. B. Sampson, “Effects of bending on the superconducting critical current density of monofilamentary Nb₃Sn wires,” *Applied Physics Letters* **36**,

223–225 (1980).

² John R. Clem and Karl K. Berggren, “Geometry-dependent critical currents in superconducting nanocircuits,” *Phys. Rev. B* **84**, 174510 (2011).

- ³ Nathaniel Allen, Philip Mallon, Joseph King, Luisa Chiesa, and Makoto Takayasu, “Wide range pure bending strains of nb3sn wires,” *Superconductor Science and Technology* **27**, 065014 (2014).
- ⁴ Tancredi Salamone, Mathias B. M. Svendsen, Morten Amundsen, and Sol Jacobsen, “Curvature-induced long-range supercurrents in diffusive superconductor-ferromagnet-superconductor Josephson junctions with a dynamic $0-\pi$ transition,” *Phys. Rev. B* **104**, L060505 (2021).
- ⁵ Tancredi Salamone, Henning G Hugdal, Morten Amundsen, and Sol H Jacobsen, “Curvature control of the superconducting proximity effect in diffusive ferromagnetic nanowires,” *Physical Review B* **105**, 134511 (2022).
- ⁶ Alv Johan Skarpeid, Henning G Hugdal, Tancredi Salamone, Morten Amundsen, and Sol H Jacobsen, “Non-constant geometric curvature for tailored spin-orbit coupling and chirality in superconductor-magnet heterostructures,” *Journal of Physics: Condensed Matter* **36**, 235302 (2024).
- ⁷ Tancredi Salamone, Magnus Skjærpe, Henning G. Hugdal, Morten Amundsen, and Sol H. Jacobsen, “Interface probe for antiferromagnets using geometric curvature,” *Phys. Rev. B* **109**, 094508 (2024).
- ⁸ Tancredi Salamone, Henning G. Hugdal, Morten Amundsen, and Sol H. Jacobsen, “Electrical control of superconducting spin valves using ferromagnetic helices,” *Applied Physics Letters* **125**, 062602 (2024).
- ⁹ Jacob Linder and Jason W. A. Robinson, “Superconducting spintronics,” *Nature Physics* **11**, 307–315 (2015).
- ¹⁰ Matthias Eschrig, “Spin-polarized supercurrents for spintronics,” *Physics Today* **64**, 43–49 (2011).
- ¹¹ Matthias Eschrig, “Spin-polarized supercurrents for spintronics: a review of current progress,” *Reports on Progress in Physics* **78**, 104501 (2015).
- ¹² Morten Amundsen, Jacob Linder, Jason W. A. Robinson, Igor Žutić, and Niladri Banerjee, “Colloquium: Spin-orbit effects in superconducting hybrid structures,” *Rev. Mod. Phys.* **96**, 021003 (2024).
- ¹³ J. W. A. Robinson, J. D. S. Witt, and M. G. Blamire, “Controlled injection of spin-triplet supercurrents into a strong ferromagnet,” *Science* **329**, 59–61 (2010).
- ¹⁴ Trupti S. Khaire, Mazin A. Khasawneh, W. P. Pratt, and Norman O. Birge, “Observation of spin-triplet superconductivity in Co-based Josephson junctions,” *Phys. Rev. Lett.* **104**, 137002 (2010).
- ¹⁵ F. S. Bergeret and I. V. Tokatly, “Singlet-triplet conversion and the long-range proximity effect in superconductor-ferromagnet structures with generic spin dependent fields,” *Phys. Rev. Lett.* **110**, 117003 (2013).
- ¹⁶ F S Bergeret and I V Tokatly, “Spin-orbit coupling as a source of long-range triplet proximity effect in superconductor-ferromagnet hybrid structures,” *Physical Review B* **89**, 134517 (2014).
- ¹⁷ Sol H Jacobsen, Jabir Ali Ouassou, and Jacob Linder, “Critical Temperature and Tunneling Spectroscopy of Superconductor-Ferromagnet Hybrids with Intrinsic Rashba–Dresselhaus Spin-Orbit Coupling,” *Physical Review B* **92**, 024510 (2015).
- ¹⁸ Paola Gentile, Mario Cuoco, Oleksii M Volkov, Zu-Jian Ying, Ivan J Vera-Marun, Denys Makarov, and Carmine Ortix, “Electronic materials with nanoscale curved geometries,” *Nature Electronics* **5**, 551–563 (2022).
- ¹⁹ Carmine Ortix, “Quantum mechanics of a spin-orbit coupled electron constrained to a space curve,” *Phys. Rev. B* **91**, 245412 (2015).
- ²⁰ Paola Gentile, Mario Cuoco, and Carmine Ortix, “Curvature-induced Rashba spin-orbit interaction in strain-driven nanostructures,” *Spin* **03**, 1340002 (2013).
- ²¹ Zu-Jian Ying, Paola Gentile, Carmine Ortix, and Mario Cuoco, “Designing electron spin textures and spin interferometers by shape deformations,” *Phys. Rev. B* **94**, 081406 (2016).
- ²² Kumar Sourav Das, Denys Makarov, Paola Gentile, Mario Cuoco, Bart J. van Wees, Carmine Ortix, and Ivan J. Vera-Marun, “Independent geometrical control of spin and charge resistances in curved spintronics,” *Nano Letters* **19**, 6839–6844 (2019).
- ²³ Denys Makarov, Oleksii M Volkov, Attila Kákay, Oleksandr V Pylypovskyi, Barbora Budinská, and Oleksandr V Dobrovolskiy, “New dimension in magnetism and superconductivity: 3d and curvilinear nanoarchitectures,” *Advanced Materials* **34**, 2101758 (2022).
- ²⁴ Vladimir M Fomin and Oleksandr V Dobrovolskiy, “A perspective on superconductivity in curved 3d nanoarchitectures,” *Applied Physics Letters* **120** (2022), 10.1063/5.0085095.
- ²⁵ A. A. Kopasov, A. G. Kutlin, and A. S. Mel’nikov, “Geometry controlled superconducting diode and anomalous Josephson effect triggered by the topological phase transition in curved proximitized nanowires,” *Phys. Rev. B* **103**, 144520 (2021).
- ²⁶ Y. Tanaka, Y. Tanuma, and A. A. Golubov, “Odd-frequency pairing in normal-metal/superconductor junctions,” *Phys. Rev. B* **76**, 054522 (2007).
- ²⁷ Zu-Jian Ying, Mario Cuoco, Carmine Ortix, and Paola Gentile, “Tuning pairing amplitude and spin-triplet texture by curving superconducting nanostructures,” *Phys. Rev. B* **96**, 100506 (2017).
- ²⁸ A. G. Kutlin and A. S. Mel’nikov, “Geometry-dependent effects in majorana nanowires,” *Phys. Rev. B* **101**, 045418 (2020).
- ²⁹ Po-Hao Chou, Chia-Hsin Chen, Shih-Wei Liu, Chung-Hou Chung, and Chung-Yu Mou, “Geometry-induced topological superconductivity,” *Phys. Rev. B* **103**, 014508 (2021).
- ³⁰ Gianluca Francica, Mario Cuoco, and Paola Gentile, “Topological superconducting phases and Josephson effect in curved superconductors with time reversal invariance,” *Phys. Rev. B* **101**, 094504 (2020).
- ³¹ Jian-Xin Zhu, *Bogoliubov-de Gennes method and its applications*, Vol. 924 (Springer, 2016).
- ³² A.N. Pressley, *Elementary differential geometry* (Springer Science & Business Media, 2010).
- ³³ Carmine Ortix, Suwit Kiravittaya, Oliver G. Schmidt, and Jeroen Van Den Brink, “Curvature-induced geometric potential in strain-driven nanostructures,” *Physical Review B* **84**, 045438 (2011).
- ³⁴ J. Bardeen and W. Shockley, “Deformation potentials and mobilities in non-polar crystals,” *Physical Review* **80**, 72–80 (1950).
- ³⁵ Chris G. Van de Walle, “Band lineups and deformation potentials in the model-solid theory,” *Physical Review B* **39**, 1871 (1989).
- ³⁶ César González-Ruano, Diego Caso, Lina G Johnsen, Coriolan Tiusan, Michel Hehn, Niladri Banerjee, Jacob Linder, and Farkhad G Aliev, “Superconductivity assisted change of the perpendicular magnetic anisotropy in V/MgO/Fe junctions,” *Scientific Reports* **11**, 19041 (2021).
- ³⁷ Jacob Linder and Alexander V. Balatsky, “Odd-frequency superconductivity,” *Rev. Mod. Phys.* **91**, 045005 (2019).
- ³⁸ Elihu Abrahams, Alexander Balatsky, D. J. Scalapino, and J. R. Schrieffer, “Properties of odd-gap superconductors,” *Phys. Rev. B* **52**, 1271–1278 (1995).
- ³⁹ Vetle Risinggård and Jacob Linder, “Direct and inverse superspin hall effect in two-dimensional systems: Electrical detection of spin supercurrents,” *Phys. Rev. B* **99**, 174505 (2019).
- ⁴⁰ John M. Blatt and Colin J. Thompson, “Shape resonances in superconducting thin films,” *Phys. Rev. Lett.* **10**, 332–334 (1963).
- ⁴¹ Yang Guo, Yan-Feng Zhang, Xin-Yu Bao, Tie-Zhu Han, Zhe Tang, Li-Xin Zhang, Wen-Guang Zhu, E. G. Wang, Qian Niu, Z. Q. Qiu, Jin-Feng Jia, Zhong-Xian Zhao, and Qi-Kun Xue, “Superconductivity modulated by quantum size effects,” *Science* **306**, 1915–1917 (2004).

- ⁴² Tai-Chang Chiang, “Superconductivity in thin films,” *Science* **306**, 1900–1901 (2004).
- ⁴³ Giovanni Alberto Ummary and Alessio Zaccone, “Can the noble metals (au, ag, and cu) be superconductors?” *Phys. Rev. Mater.* **8**, L101801 (2024).
- ⁴⁴ Kjell Søren Heinrich, *Curvature-Induced Phenomena in Superconductors and Josephson Junctions*, Master’s thesis, NTNU (2024).
- ⁴⁵ Jorge Cayao and Annica M. Black-Schaffer, “Odd-frequency superconducting pairing in junctions with Rashba spin-orbit coupling,” *Phys. Rev. B* **98**, 075425 (2018).
- ⁴⁶ B. Kundys, “Photostrictive materials,” *Applied Physics Reviews* **2**, 011301 (2015).
- ⁴⁷ B.D. Josephson, “Possible new effects in superconductive tunnelling,” *Physics Letters* **1**, 251–253 (1962).
- ⁴⁸ Michael Tinkham, *Introduction to Superconductivity*, 2nd edition (Dover publications, 1996).
- ⁴⁹ Hervé Bulou, Loïc Joly, Jean-Michel Mariot, and Fabrice Scheurer, *Magnetism and Accelerator-Based Light Sources* (Springer Nature, 2021).
- ⁵⁰ V. V. Ryazanov, V. A. Oboznov, A. Yu. Rusanov, A. V. Veretennikov, A. A. Golubov, and J. Aarts, “Coupling of two superconductors through a ferromagnet: Evidence for a π junction,” *Phys. Rev. Lett.* **86**, 2427–2430 (2001).
- ⁵¹ T. Kontos, M. Aprili, J. Lesueur, F. Genêt, B. Stephanidis, and R. Boursier, “Josephson junction through a thin ferromagnetic layer: Negative coupling,” *Phys. Rev. Lett.* **89**, 137007 (2002).
- ⁵² Norman O. Birge and Nathan Satchell, “Ferromagnetic materials for Josephson π junctions,” *APL Materials* **12**, 041105 (2024).
- ⁵³ J.J.A. Baselmans, A.F. Morpurgo, B.J. van Wees, and T.M. Klapwijk, “Reversing the direction of the supercurrent in a controllable Josephson junction,” *Nature* **397**, 43–45 (1999).
- ⁵⁴ Yue Mao and Qing-Feng Sun, “Spin phase regulated spin josephson supercurrent in topological superconductor,” *Phys. Rev. B* **105**, 184511 (2022).
- ⁵⁵ Yue Mao, Qing Yan, Yu-Chen Zhuang, and Qing-Feng Sun, “Universal spin superconducting diode effect from spin-orbit coupling,” *Phys. Rev. Lett.* **132**, 216001 (2024).
- ⁵⁶ Sol H. Jacobsen, Iryna Kulagina, and Jacob Linder, “Controlling superconducting spin flow with spin-flip immunity using a single homogeneous ferromagnet,” *Scientific Reports* **6**, 23926 (2016).
- ⁵⁷ A Manchon, H C Koo, J Nitta, S M Frolov, and R A Duine, “New perspectives for Rashba spin-orbit coupling,” *Nature Materials* **14**, 871–882 (2015).
- ⁵⁸ V.M. Edelstein, “Spin polarization of conduction electrons induced by electric current in two-dimensional asymmetric electron systems,” *Solid State Communications* **73**, 233–235 (1990).
- ⁵⁹ R. Trotta, P. Atkinson, J. D. Plumhof, E. Zallo, R. O. Rezaev, S. Kumar, S. Baunack, J. R. Schröter, A. Rastelli, and O. G. Schmidt, “Nanomembrane quantum-light-emitting diodes integrated onto piezoelectric actuators,” *Advanced Materials* **24**, 2668–2672 (2012).
- ⁶⁰ Tancredi Salamone, Henning G. Hugdal, Sol H. Jacobsen, and Morten Amundsen, “High magnetic field superconductivity in a two-band superconductor,” *Phys. Rev. B* **107**, 174516 (2023).
- ⁶¹ GI González-Pedrerros, JA Camargo-Martínez, and F Mesa, “Cooper pairs distribution function for bcc Niobium under pressure from first-principles,” *Scientific Reports* **11**, 7646 (2021).
- ⁶² Ruslan Prozorov, Mehdi Zarea, and James A Sauls, “Niobium in the clean limit: An intrinsic type-I superconductor,” *Physical Review B* **106**, L180505 (2022).
- ⁶³ D Bonnet, S Erlenkämper, H Germer, and H Rabenhorst, “A new measurement of the energy gap in superconducting niobium,” *Physics Letters A* **25**, 452–453 (1967).